

Three-dimensional diffuse optical tomography of osteoarthritis: initial results in the finger joints

Zhen Yuan

Qizhi Zhang

University of Florida
Department of Biomedical Engineering
Gainesville, Florida 32611-6131

Eric Sobel

University of Florida
Division of Rheumatology
College of Medicine
Gainesville, Florida 32611

Huabei Jiang

University of Florida
Department of Biomedical Engineering
Gainesville, Florida 32611-6131
E-mail: hjiang@bme.ufl.edu

Abstract. This work presents a pilot study to show the potential of an emerging imaging modality, near-infrared diffuse optical tomography (DOT), for the diagnosis of osteoarthritis (OA). We report quantitative absorption and scattering images of joint tissue that allow for differentiation between diseased and healthy joints. An automatic, multi-channel optical imaging system is used to image finger joints from two OA patients and three healthy volunteers. 3-D optical images of the joint tissue are recovered using a finite-element-based reconstruction algorithm. The reconstructed images demonstrate differences in optical properties at the joint region (cartilage/synovial fluid) between the OA and healthy joints. Quantitative analysis from the patients and healthy volunteers also indicate that the recovered joint sizes are consistent with those from x-ray findings. The results of this pilot study show potential for quantitative imaging and diagnosis of early OA by DOT. © 2007 Society of Photo-Optical Instrumentation Engineers. [DOI: 10.1117/1.2737420]

Keywords: finger joint; osteoarthritis; diffuse optical imaging; reconstruction algorithm; finite element method.

Paper 06078RR received Mar. 30, 2006; revised manuscript received Feb. 6, 2007; accepted for publication Feb. 22, 2007; published online May 21, 2007.

1 Introduction

Osteoarthritis (OA) is the most common joint problem worldwide and is estimated to affect nearly 60 million Americans. Although a number of factors contribute to its development, including obesity, trauma, and genetic predisposition, the hallmark of osteoarthritis is progressive damage to articular cartilage.¹ This specialized cartilage, found at the articular surface of diarthrodial joints, consists of chondrocytes imbedded within a matrix of collagens, proteoglycans, and proteinases, and provides a smooth, low-friction surface for movement. As damage progresses, the chondrocytes lose their ability to synthesize a high-quality matrix. Fissuring of the articular cartilage can result in fragmentation and deposition of small loose bodies within the joint space. Typically, a low-grade inflammatory reaction occurs, and the synovial fluid may lose some of its normal viscoelastic and lubricating properties. Subchondral bone becomes exposed and results in sclerosis. In response to these stresses, there is typically new bone formation, termed osteophytes, which are preferentially found at the joint margins. Classically, OA is most often found in the large weight-bearing joints of the lower extremities, particularly the knees and hips. However, there is also a subset of individuals with a predilection for developing OA of the hands and a more generalized form of OA.² Interestingly, it is the distal and proximal interphalangeal joints that are most often affected and culminate in the development of Heberden's (distal) and Bouchard's (proximal) nodes.

Although current therapy is symptomatic, remarkable advances have been made in our understanding of the pathophysiology of OA.³⁻⁵ Much of the degradation of cartilage is mediated through matrix metalloproteinases, and the development of small-molecule inhibitors has been an area of active research interest.⁶⁻⁸ In anticipation of the development of new products with the potential to alter the natural history of OA, it will be crucial to have noninvasive technologies that can detect early OA and monitor efficacy of therapy.

To diagnose cartilage abnormalities and alterations in composition of synovial fluid in joints affected by OA, a variety of imaging methods have been developed and tested, such as radiography (x-ray), ultrasound (US), computed tomography (CT), and magnetic resonance imaging (MRI).⁹⁻¹³ Of all of the imaging modalities, the best established is x-ray. However, while plain radiographs are able to visualize joint space narrowing and osteophyte formation, they are insensitive to changes in cartilage and fluid and therefore incapable of capturing the primary features of the early stages of OA.¹⁴ MRI, another commonly used modality in clinical practice, can reliably detect early OA when high contrast agents are used. However, it is costly and time consuming.¹⁵ Computed tomography (CT) has also been employed in the diagnosis of OA. However, it too is very expensive and provides only qualitative structural information in severe OA.⁹ Musculoskeletal ultrasound has been the subject of much recent interest in evaluating rheumatoid arthritis and regional musculoskeletal pathology.^{8,10,16,17} A strongly operator-dependent modality and sensitive only to changes in the boundary layer, it has

Address all correspondence to Huabei Jiang, Department of Biomedical Engineering, University of Florida, 137 BME Building—PO Box 116131, Gainesville, FL 32611-6131 United States of America; Tel: 352-392-7943; Fax: 352-392-9791; E-mail: hjiang@bme.ufl.edu

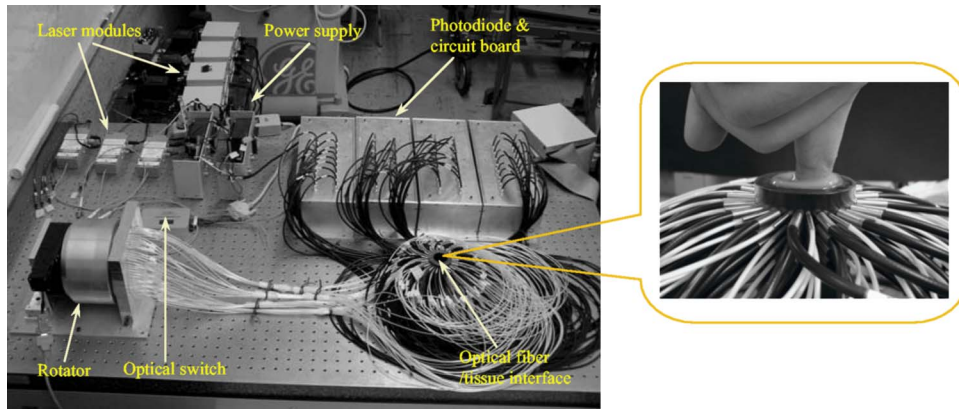


Fig. 1 Photograph of the DOT imaging system. The insert is a close-view photograph of the finger/coupling medium/fiber optics interface.

limited utility in evaluation of the early stages of OA, at a time when there has been little change in joint space.¹⁸

As an emerging nonionizing technology, near-infrared optical imaging has received much attention because optical techniques offer unique advantages over the existing imaging methods mentioned. Optical imaging is low in cost and non-invasive. Besides the advantages of utilizing only low-level and nonionizing near-infrared radiation, it can be realized in compact, portable instruments. Moreover, the imaging contrast offered by diffuse optical tomography is high, suggesting a possible use in early OA detection. Ultimately, optical imaging methods are able to provide a variety of functional and structural information with high sensitivity and specificity compared to other imaging modalities. This is especially true for the joints of the fingers, where the small dimensions and much higher transmitted light intensities should result in better signal-to-noise ratios and greatly improved spatial resolution.

Three typical optical techniques are currently being used for optical tissue imaging: continuous-wave, time-resolved, and frequency-domain methods. Most of these studies have been focused on direct image formulation from the measured optical data, which may not fully exploit all of the information provided. In consideration of the advantages over direct imaging methods, several groups are now concentrating on model-based diffuse optical tomography (DOT) methods,^{19–21} in which the diffusion approximation to model light propagation in tissue is used for multiply scattered light. Due to the use of an effective reconstruction algorithm, DOT is able to improve the resolution limitation and to detect deep tissues. Phantom and clinical experiments have shown that the diffuse optical reconstruction method is able to recover both structural and functional information from brain and breast tissues.¹⁹ Recent phantom and clinical studies showed that DOT can also provide quantitative images of joints and associated bones.²² For example, Xu, Iftimia, and Jiang²³ first reported the DOT imaging of healthy finger joints. Schwaighofer et al.,²⁴ Scheel et al.,²⁵ and Hielscher et al.²¹ demonstrated that optical tomography could be used to detect and quantitate the degree of inflammation within the finger joints of individuals with rheumatoid arthritis. Studies have indicated that the optical properties of healthy and diseased joint tissues are quite different.^{26,27} The goal of this work is to

describe an integrated 3-D DOT imaging system and reconstruction algorithm that has the potential to monitor and diagnose early osteoarthritis based on our previous phantom and *in-vivo* experiments.^{20,23}

In this study, we demonstrate that DOT imaging could distinguish between normal and degenerative joints. Besides the introduction of the imaging measurement system and reconstruction algorithm, we discuss in detail the radiographic appearance of two patients with OA and three healthy volunteers, based on qualitative optical images and quantitative optical properties. Moreover, we measured the thickness of cartilage and fluid in the distal interphalangeal (DIP) finger joint using a fitting method, which provides the structural size information to detect early changes of OA. Finally, the optical tomography images are also compared with x-ray findings.

2 Experimental Materials and Methods

2.1 Optical Imaging

All the experiments with human subjects were performed by our recently developed multichannel (64 sources and 64 detectors) photodiodes-based DOT system,^{28,29} shown in Fig. 1. The system consisted of laser modules, a hybrid light delivery subsystem, a fiber optics/tissue interface, light detection modules, and a data acquisition module.

While the system has eight diode lasers (B&W TEK Incorporated, Delaware and Power Technology Incorporated, Arkansas) with wavelengths from 634 to 974 nm acting as light sources, this study was based on the laser at 853 nm with a maximum output of 210 mW. The light intensity was measured as 70 mW when it was delivered to the fiber optical interface, and further reduced to 10 to 30 mW at the surface of the finger, which depended on the location of the finger relative to an excitation source position. An efficient and low-cost hybrid subsystem that included a 1×8 optical switch (VX500, Dicon Fiberoptics Incorporated, California) and a motorized rotator (RT-5-M17, Newmark Systems Incorporated, California) was designed to deliver laser light to excitation points on the fiber optics/tissue interface. The motorized rotator drove an optical fiber, called a laser source fiber (LS fiber), to 64 positions to transfer the light beam into 64 source fiber bundles (1 mm in diameter, 0.55 NA, RoMack

Incorporated, Virginia) that were circularly arranged. At each position, light from the laser module was coupled into the LS fiber via the optical switch.

A cylindrical fiber optics/tissue interface was employed in our study, where 64 source fiber bundles and 64 detector fiber bundles (2 mm in diameter, 0.55 NA, RoMack Incorporated, Virginia) were positioned in four layers with a 5.0-mm distance between two adjacent layers. In each layer, 16 source fiber bundles and 16 detection fiber bundles were alternatively placed with 11.25 deg intervals. A total volume with 15 mm height and 30 mm diameter was covered by these four layers, and the subject's finger joints were located inside it. To hold the finger as well as satisfy the diffusion equation, the space between the finger and the plexiglas wall that was used to hold the source/detector fiber bundles was filled with a tissue-like phantom made from water, agar, Indian Ink, and Intralipid (Fig. 1). This tissue-like medium can be solidified when its temperature is under 40 °C. After the subject placed her/his finger into the cylinder, the medium was poured in and quickly solidified within a couple of minutes. The phantom materials were chosen so that the optical properties (especially the absorption and scattering coefficients) of these phantoms were close to those of soft tissue in human fingers. Here the absorption and scattering coefficients of the phantom were 0.014/mm and 1.0/mm, respectively.

We chose 64 low noise integrated silicon-photodiodes (S8745, Hamamatsu, New Jersey) for parallel signal collection. A total of four homemade programmable circuit boards controlled all of these detector units, which were mounted into four metal boxes. The electric noise level of each sensor unit was 1.0 mV. For the wavelength range of 634 to 974 nm, the sensitivity of the S8745 silicon photodiode was between 0.34 and 0.52 V/nW, and the noise equivalent power of this system was calculated to be 2.9 to 1.9 pW. The four gain levels for each detector unit was automatically selected via a PCI-DDA02/12 output board (Measurement Computing, Massachusetts) and therefore the dynamic range of the measurement had been extended to 2.7×10^8 . Data acquisition was performed via a single 16-bit A/D board with a 200 kS/s maximum ADC rate (PCI-DA6035, Measurement Computing, Massachusetts). Data acquisition from one and eight wavelengths took about 5 and 27 minutes, respectively. The system was also carefully calibrated through a two-step calibration procedure.³⁰ An IBM Pentium 4 PC controlled the whole DOT system utilizing the LabView program. The optical switch and the motorized rotator were controlled through the parallel port and RS232 serial port, respectively.

2.2 Reconstruction Methods

Since our 3-D reconstruction algorithm has been described in detail elsewhere,^{31–33} we give a brief outline here to incorporate a recently developed numerical strategy for improved performance.²⁹ Our existing reconstruction algorithm is based on the following diffusion equation and type-3 BCs:

$$\nabla \cdot D(r) \nabla \Phi(r) - \mu_a(r)\Phi(r) = -S(r), \quad (1)$$

$$-D \nabla \Phi \cdot n = \alpha \Phi, \quad (2)$$

where $\Phi(r)$ is the photon density, $D(r)$ the diffusion coefficient, α is a coefficient related to the internal reflection at the boundary, $\mu_a(r)$ is the absorption coefficient, and $S(r)$ is the source term. For the point source model, $S=S_0\delta(r-r_0)$ is used, where S_0 is the source strength and $\delta(r-r_0)$ is the Dirac delta function for a source at r_0 . The diffusion coefficient can be written as $D=1/[3(\mu_a+\mu'_s)]$, where μ'_s is the reduced scattering coefficient. Moreover, $\Phi(r)$, D , and μ_a are spatially discretized as,

$$\Phi = \sum_{i=1}^N \Phi_i \phi_i, \quad D = \sum_{i=1}^N D_i \phi_i, \quad \mu_a = \sum_{i=1}^N (\mu_a)_i \phi_i, \quad (3)$$

where N is the node number of the 3-D finite element mesh and ϕ_i is the basis function. The discretized form of Eqs. (1) and (2) can be written as

$$[\mathbf{A}]\{\Phi\} = \{\mathbf{b}\}, \quad (4)$$

where the elements of the matrix $[\mathbf{A}]$ are

$$\alpha_{ij} = \int_V (-D \nabla \phi_j \cdot \nabla \phi_i - \mu_a \phi_j \phi_i) dV + \int_{\Gamma} (-\alpha \phi_j \phi_i) d\Gamma$$

and the integrations are performed over the problem domain (V) and boundary domain (Γ). $\{\mathbf{b}\}$ is the source vector. The inverse solution is obtained through the following equations:

$$[\mathbf{A}]\{\partial\Phi/\partial\chi\} = \{\partial\mathbf{b}/\partial\chi\} - [\partial\mathbf{A}/\partial\chi]\{\Phi\}, \quad (5)$$

$$(\mathcal{J}^T \mathcal{J} + \lambda \mathbf{I}) \Delta \chi = \mathcal{J}^T (\Phi^o - \Phi^c), \quad (6)$$

where χ expresses D and μ_a , and \mathcal{J} is the Jacobian matrix formed by $\partial\Phi/\partial\chi$ at the boundary measurement sites. λ is a scalar and \mathbf{I} is the identity matrix. $\Delta \chi = (\Delta D_1, \Delta D_2, \dots, \Delta D_n, \Delta \mu_{a,1}, \Delta \mu_{a,2}, \dots, \Delta \mu_{a,N})^T$, and $\Delta \chi$ is the updating vector for the optical properties. $\Phi^o = (\Phi_1^o, \Phi_2^o, \dots, \Phi_M^o)^T$ and $\Phi^c = (\Phi_1^c, \Phi_2^c, \dots, \Phi_M^c)^T$, where Φ_i^o and Φ_i^c are observed and computed photon densities for $i = 1, 2, \dots, M$ boundary locations.

The existing reconstruction process involves the iterative solution of Eqs. (4)–(6): an update of optical property distribution is obtained at each iteration, i.e., $\chi_{\text{new}} = \chi_{\text{old}} + \Delta \chi$. To obtain better reconstructions especially for highly heterogeneous media such as finger joints, a globally convergent method³⁴ for nonlinear systems of equations was employed here. A global method is one that converges to a solution from almost any starting point. The actual update for a globally convergent reconstruction method is determined by the following equation,

$$\chi_{\text{new}} = \chi_{\text{old}} + \lambda' \Delta \chi \quad (0 < \lambda' \leq 1), \quad (7)$$

where λ' is computed from a backtracking line search.^{29,34} Thus in DOT, the image formation task for the finger joint is to update D and μ_a distributions via an iterative solution of Eqs. (4)–(7), so that a weighted sum of the squared differences between computed and measured data can be minimized.

2.3 X-Ray Imaging

As a conventional technology for diagnosing osteoarthritis, plain radiographs can provide high quality structural images of the bones of a joint. To compare the findings from the recovered optical images with those obtained from x-ray images, radiographs were taken for each subject's finger joints. All the digital x-ray images presented in this work were taken by a Mini C-arm x-ray system (MiniView 6800, GE-OEC, Utah) with $1\text{ k} \times 1\text{ k} \times 16$ -bit image processing. The exposure dose was lower than 10 mRad per projection when the exposure time was 2 s, and the x-ray tube worked at 50 kVp and $35\ \mu\text{A}$. The fingers were placed about 90 mm above the detector, while the distance between the x-ray tube and detector was 450 mm. Therefore, the real size of a joint could be calculated by applying a factor of 4/5.

Since conventional radiographs are only 2-D projections of the body's 3-D structure, digital tomosynthesis was employed to create a 3-D image of the finger joint from 2-D x-ray projections to show the exact position and orientation of the joints, so that better comparison with the optical imaging could be performed. The 3-D x-ray images were reconstructed using an improved shift-and-add algorithm from 16 projections³⁵ and displayed with commercial software called AMIRA.³⁶

2.4 Patient Examinations

Five persons including two patients and three healthy volunteers were recruited from the hospital and university campus. The clinical study was approved by the University Institutional Review Board, and the volunteers gave informed consent prior to investigation. All the diseased joints were examined by a physician and showed clear signs of OA. For the two patients we scanned, they had difficulty in moving their fingers smoothly and suffered from pain within their finger joint during movement. Their situation went worse in cold weather. Joint space narrowing was clearly observed.

The reconstruction of the DIP joint with the coupling phantoms (30 mm in diameter and 20 mm in height) was performed with a mesh of 3009 nodes and 12,800 tetrahedral elements. 64 sources and 64 detectors were distributed uniformly along the surface of the phantom at four planes ($z = 2.5, z = 7.5, z = 12.5,$ and $z = 17.5$ mm; 16 sources and 16 detectors at each plane). The initial guesses used for the reconstruction were $\mu'_s = 1.0/\text{mm}$, $\mu_a = 0.03/\text{mm}$, $S = 9.8$, and $\alpha = 0.001$. The reconstruction took about 2 h on a 1-GHz Pentium 4 PC with about 20 iterations.

Because structural size information is also an important measure of the degree of OA,^{37,38} besides the recovered optical properties, a novel fitting algorithm is developed to assess the thickness of cartilage and synovial fluid from DOT imaging in consideration of the following points: 1) the gradient for image intensity exists between the bones and joint tissues; 2. the fluid thickness is much thinner than the cartilage; 3. it only makes sense for computing average thickness of gap and cartilage tissues because joint thickness is position dependent. The proposed fitting algorithm, called the full-width at 30% maximum (FW30%M) method, was able to calculate the quantitative structural size of joint tissues.

For the FW30%M method, we first took six representative dorsal and coronal slices (three x - z slices and three y - z slices)

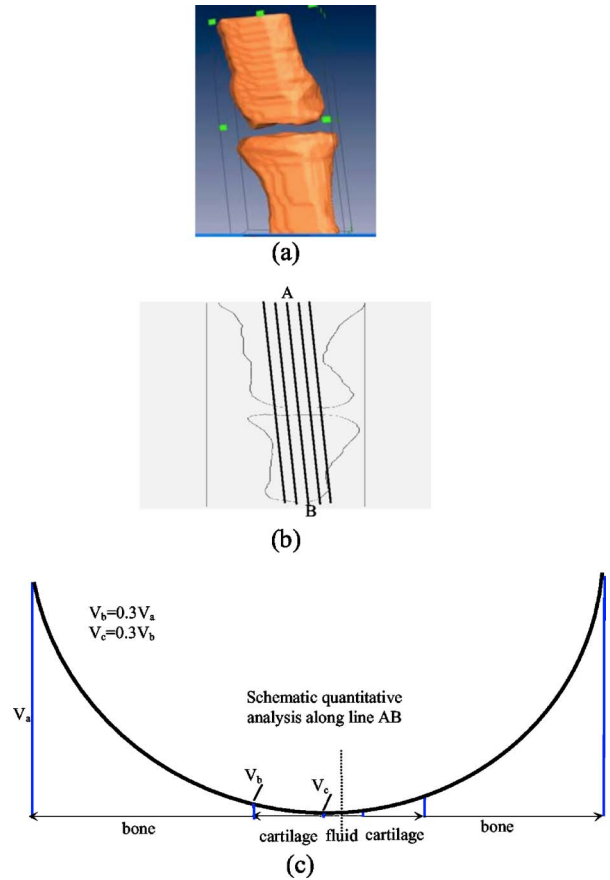


Fig. 2 (a) 3-D schematic of the finger joint measurement configuration. (b) Schematic of 2-D dorsal/coronal slice along with the five lines used for quantitative analysis. (c) Schematic of a 2-D optical property profile along line AB shown in (b). $V_{a,b,c}$ indicates optical property value at different points along the profile.

from the reconstructed 3-D image for quantitative analysis, which included two central slices in dorsal and coronal planes, respectively. The six slices chosen were different for each patient. For instance, for OA patient 1, the three dorsal slices were taken at $y = -1, 0,$ and 1 mm, and the three coronal slices were taken at $x = -3, -1,$ and 1 mm. The distance between two adjacent slices was about 1 to 2 mm. While the central dorsal and coronal slices go from -15 to 15 mm, the width of the other four slices is smaller than that of the central ones.

For each slice, we plotted five central lines for quantitative analysis of absorption and scattering properties, as shown in schematic Figs. 2(a) and 2(b). We limited the five lines within the finger domain. These lines were not always vertical, and for some cases we used lines that were tilted and parallel to the middle line of the bones. Thus we were able to ensure that the schematic curves shown in Fig. 2(c) really represented actual slices from the side-to-side 2-D images. The full width at 30% maximum curve for each line was divided into three parts: bone, cartilage, and fluid. The interface points among bone, cartilage, and fluid were taken as 30% of the nearest highest values on the curves, as shown in schematic Fig. 2(c). In this study, quantitative analysis was conducted for 30 central lines located on six slices of each recovered 3-D image.

Table 1 Reconstructed scattering related parameters for five cases. Note that u_{a-c} , u_{a-f} , and u_{a-b} are the absorption coefficients of cartilage, fluid, and bone, respectively. u'_{s-c} , u'_{s-f} , and u'_{s-b} are the scattering coefficients of cartilage, fluid, and bone, respectively.

	Case	Joint tissues	Averaged u'_s (1/mm)	Mean thickness (mm)	X-ray size (mm)	u'_{s-c}/u'_{s-b}	u'_{s-f}/u'_{s-b}
OA	1	Bone	2.30	N/A	N/A	0.843	0.796
		Cartilage	1.94	1.0	0.75		
		Fluid	1.83	0.3	N/A		
	2	Bone	1.67	N/A	N/A	0.719	0.599
		Cartilage	1.20	1.1	0.78		
		Fluid	0.99	0.4	N/A		
Healthy	3	Bone	1.96	N/A	N/A	0.622	0.469
		Cartilage	1.22	1.7	1.46		
		Fluid	0.92	0.6	N/A		
	4	Bone	1.51	N/A	N/A	0.675	0.536
		Cartilage	1.02	1.7	1.21		
		Fluid	0.81	0.6	N/A		
	5	Bone	1.45	N/A	N/A	0.666	0.531
		Cartilage	0.97	1.9	1.42		
		Fluid	0.77	0.6	N/A		

By using this threshold, we calculated the mean thickness of cartilage as well as fluid, and we also provided the averaged optical properties of bone, cartilage, and fluid. The quantitative results for the scattering coefficients were given in Table 1 and the absorption properties are listed in Table 2. Further, it should be noted that for the developed fitting algorithm we used the joint space measured from the x-ray images of healthy joints as the standard to determine the criteria value for estimating the geometrical sizes of joint tissues from the optical images. We found 30% at maximum gave us the best results relative to x-ray. Additionally, the difference between different slices surely existed, but we calculated the mean values of different slices to reduce the error. Finally, the mean structural sizes of joints from the high-resolution x-ray images were provided in Tables 1 and 2 for comparison.

2.4.1 Case 1: osteoarthritis patient 1

This patient was a 50-year-old female, who was first diagnosed with OA in both joints of the index finger about 10 years ago. Figures 3(a) and 3(b) plot the longitudinal scattering slices (along both x and y coordinates) of a recovered 3-D image for patient 1. Figures 3(c) and 3(d) display the reconstructed longitudinal absorption slices for this patient. The x-ray findings are given in Fig. 3(e). The 3-D tomosynthesis x-ray image is also given later for case 1 to show the exact position and orientation of the joint. The structural size of the joint, including the fluid and cartilage, is calculated and

listed in Tables 1 and 2, where the average optical properties of bone and cartilage as well as fluid are also provided.

2.4.2 Case 2: osteoarthritis patient 2

The second patient was also a 50-year-old female, whose DIP joint developed clinical OA about 4 years ago. Figures 4(a) and 4(b) plot the recovered scattering slices of the 3-D image for this patient. Figures 4(c) and 4(d) provide the reconstructed longitudinal absorption slices for the 3-D representation of this joint. We also computed the recovered structural sizes and optical properties of the joint, and these quantitative results are given in Tables 1 and 2 for this patient. An x-ray image for patient 2 is presented in Fig. 4(e). The tomosynthesis x-ray image for case 2 is provided later.

2.4.3 Case 3: healthy volunteers

The ages of the healthy volunteers shown as cases 3 to 5 ranged from 32 to 40. Figures 5(a) and 5(b) display the recovered longitudinal scattering slices for case 3. The reconstructed absorption slices are given in Figs. 5(c) and 5(d). The reconstructed mean absorption and scattering properties as well as structural sizes are presented in Tables 1 and 2. Moreover, an x-ray image is provided to compare with the optical tomography images for the healthy volunteer, as shown in Fig. 5(e). The tomosynthesis x-ray image for case 3 is displayed in Fig. 6(c), cases 1 and 2 in Figs. 6(a) and 6(b), respectively.

Table 2 Reconstructed absorption related parameters for five cases. Note that u_{a-c} , u_{a-fr} , and u_{a-b} are the absorption coefficients of cartilage, fluid, and bone, respectively. u'_{s-c} , u'_{s-fr} , and u'_{s-b} are the scattering coefficients of cartilage, fluid, and bone, respectively.

	Case	Joint tissues	Averaged μ_a (1/mm)	Mean thickness (mm)	X-ray size (mm)	u_{a-c}/u_{a-b}	u_{a-fr}/u_{a-b}
OA	1	Bone	0.0526	N/A	N/A	0.859	0.817
		Cartilage	0.0452	1.0	0.75		
		Fluid	0.0430	0.3	N/A		
	2	Bone	0.055	N/A	N/A	0.836	0.782
		Cartilage	0.046	1.1	0.78		
		Fluid	0.043	0.4	N/A		
Healthy	3	Bone	0.0513	N/A	N/A	0.657	0.534
		Cartilage	0.0337	1.8	1.46		
		Fluid	0.0274	0.5	N/A		
	4	Bone	0.0796	N/A	N/A	0.628	0.500
		Cartilage	0.0500	1.3	1.21		
		Fluid	0.0398	0.4	N/A		
	5	Bone	0.0560	N/A	N/A	0.559	0.414
		Cartilage	0.0313	1.5	1.42		
		Fluid	0.0232	0.5	N/A		

3 Discussion

In this pilot clinic evaluation of an optical imaging system for OA of the hand, we obtained two types of imaging parameters, including optical properties and the structural sizes of cartilage and fluid. Physically, these quantitative results represent two different intrinsic properties of the finger joint and can be employed to diagnose and monitor the progression of early OA.

We first examine the qualitative images shown in Figs. 3–5. From these absorption and scattering images, we immediately note that the bones are clearly delineated (most red color regions) for both OA and normal joints, where we also see that the shape and size of the bones are better recovered in the absorption images than those in the scattering images. While there is no clear boundary between the bones and cartilage/fluid, the joint tissue/space is clearly identified. Here, the joint space narrowing seems apparent for both OA joints (Figs. 3 and 4) relative to the healthy joints (Fig. 5), and this narrowing appears to be stronger for the more advanced OA joint (patient 1, Fig. 3). Importantly, we note that the distributions of both absorption and scattering coefficients in the joint space are highly heterogeneous, especially for the advanced OA joint (e.g., see Fig. 3), while such distributions are quite homogeneous in general for the healthy joints (e.g., see Fig. 5).

We now discuss the quantitative results given in Tables 1 and 2. We note from Table 1 that the scattering value of the

diseased fluid for both OA cases ($\mu'_s=1.83/\text{mm}$ and $0.99/\text{mm}$) are larger than that of the healthy fluid ($\mu'_s=0.92, 0.81$, and $0.77/\text{mm}$), with the advanced OA case having the largest value ($\mu'_s=1.83/\text{mm}$). While the scattering coefficient value of cartilage for the advanced OA joint is the largest, we see that this value for OA patient 2 is slightly smaller than that for healthy case 3, but larger than that for other healthy cases. Interestingly, the difference in scattering coefficient of joint tissues between the OA and healthy controls seems apparent from the ratio of this optical property of cartilage and fluid to that of bone (the last two columns in Table 1). We immediately note that this ratio for both diseased cartilage and fluid is larger than that for normal cartilage and fluid. Furthermore, as shown in Table 1, the mean thickness of cartilage and fluid for cases 1 and 2 are 1.0 and 0.3 mm, and 1.1 and 0.4 mm, respectively. However, the mean thickness of cartilage and fluid for cases 3, 4, and 5, are 1.7 and 0.6 mm, 1.7 and 0.6 mm, and 1.9 and 0.6 mm, respectively. Compared with the normal controls, the two patients with OA appear to show joint space narrowing by our technique.

Similar observations can be made regarding the quantitative results listed in Table 2 for absorption coefficient images. We see from Table 2 that the absorption value of the diseased fluid for both OA cases ($\mu_a=0.043/\text{mm}$) is larger than that of the healthy fluid ($\mu_a=0.0274, 0.0398$, and $0.0232/\text{mm}$). We note, however, that the absorption coefficient values of the

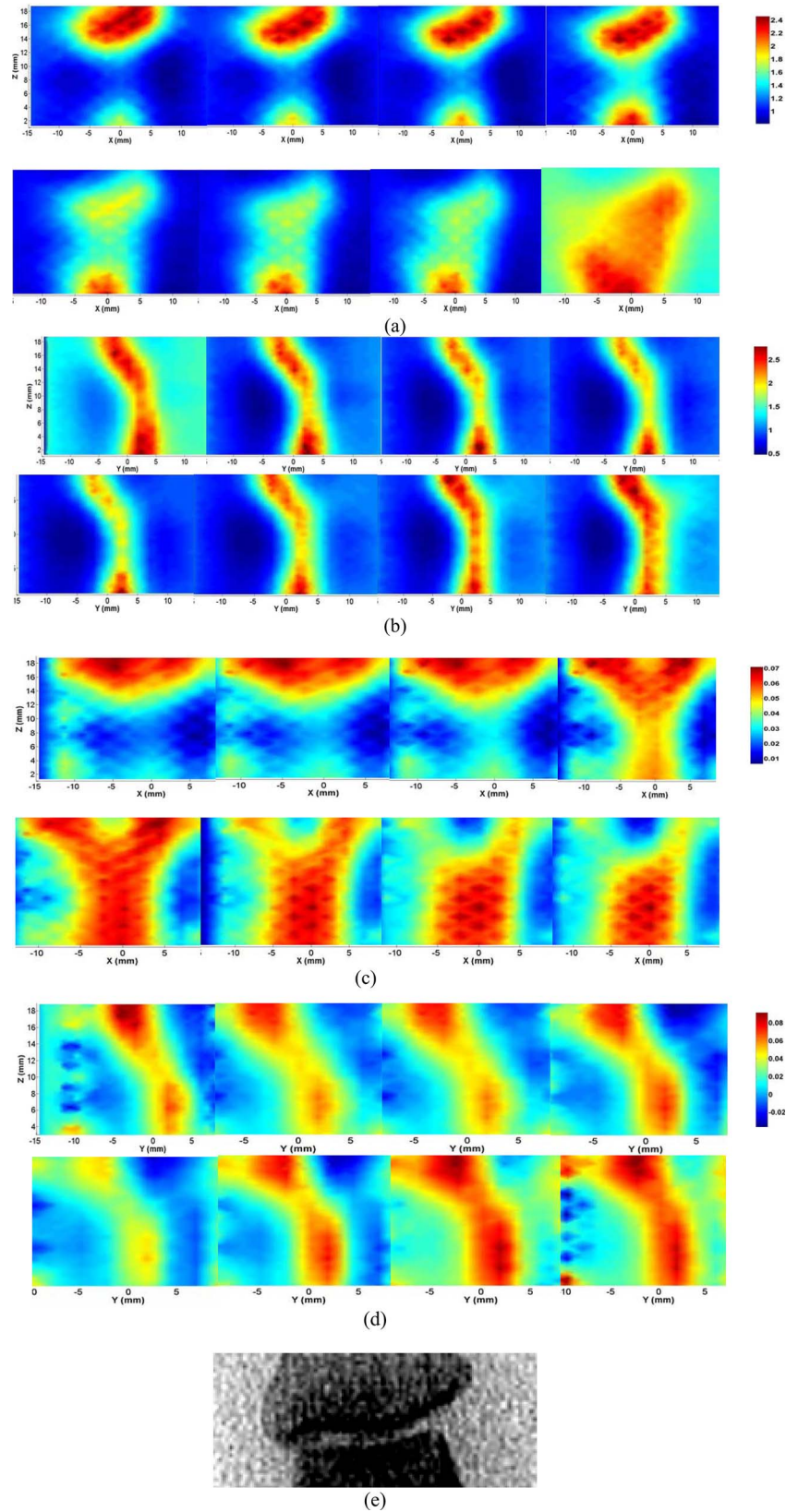


Fig. 3 Reconstructed images at selected dorsal/coronal planes for case 1: (a) scattering slices at $y = -2, -1.5, -1, -0.5, 0, 1, 2,$ and 2.5 mm (dorsal planes); (b) scattering slices at $x = -5, -4, -3, -2, -1, 0, 1,$ and 2 mm (coronal planes); (c) absorption slices at $y = -2, -1.5, -1, -0.5, 0, 1, 2,$ and 2.5 mm (dorsal planes); (d) absorption slices at $x = -5, -4, -3, -2, -1, 0, 1,$ and 2 mm (coronal planes); and (e) x-ray image. The axes (left and bottom) indicate the spatial scale in millimeters, whereas the color scale gives the absorption or scattering coefficient in inverse millimeters.

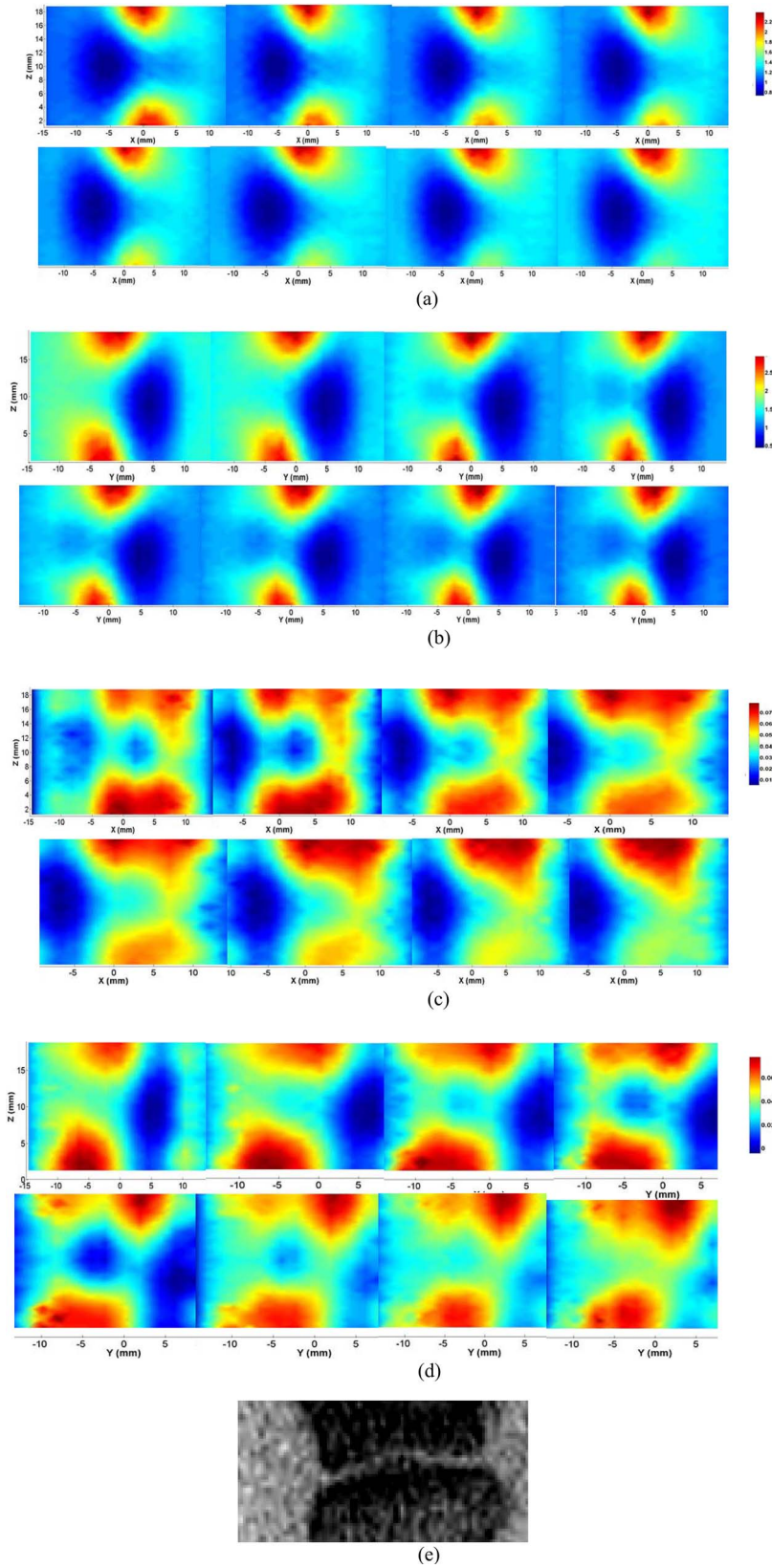


Fig. 4 Reconstructed images at selected dorsal/coronal planes from case 2: (a) scattering slices at $y = -3, -2, -1, -0.5, 0, 1, 1.5,$ and 2 mm (dorsal planes); (b) scattering slices at $x = -1.5, -1, -0.5, 0, 0.5, 1.0, 1.5,$ and 2 mm (coronal planes); (c) absorption slices at $y = -3, -2, -1, -0.5, 0, 1, 1.5,$ and 2 mm (dorsal planes); (d) absorption slices at $x = -1.5, -1, -0.5, 0, 0.5, 1.0, 1.5,$ and 2 mm (coronal planes); and (e) x-ray image.

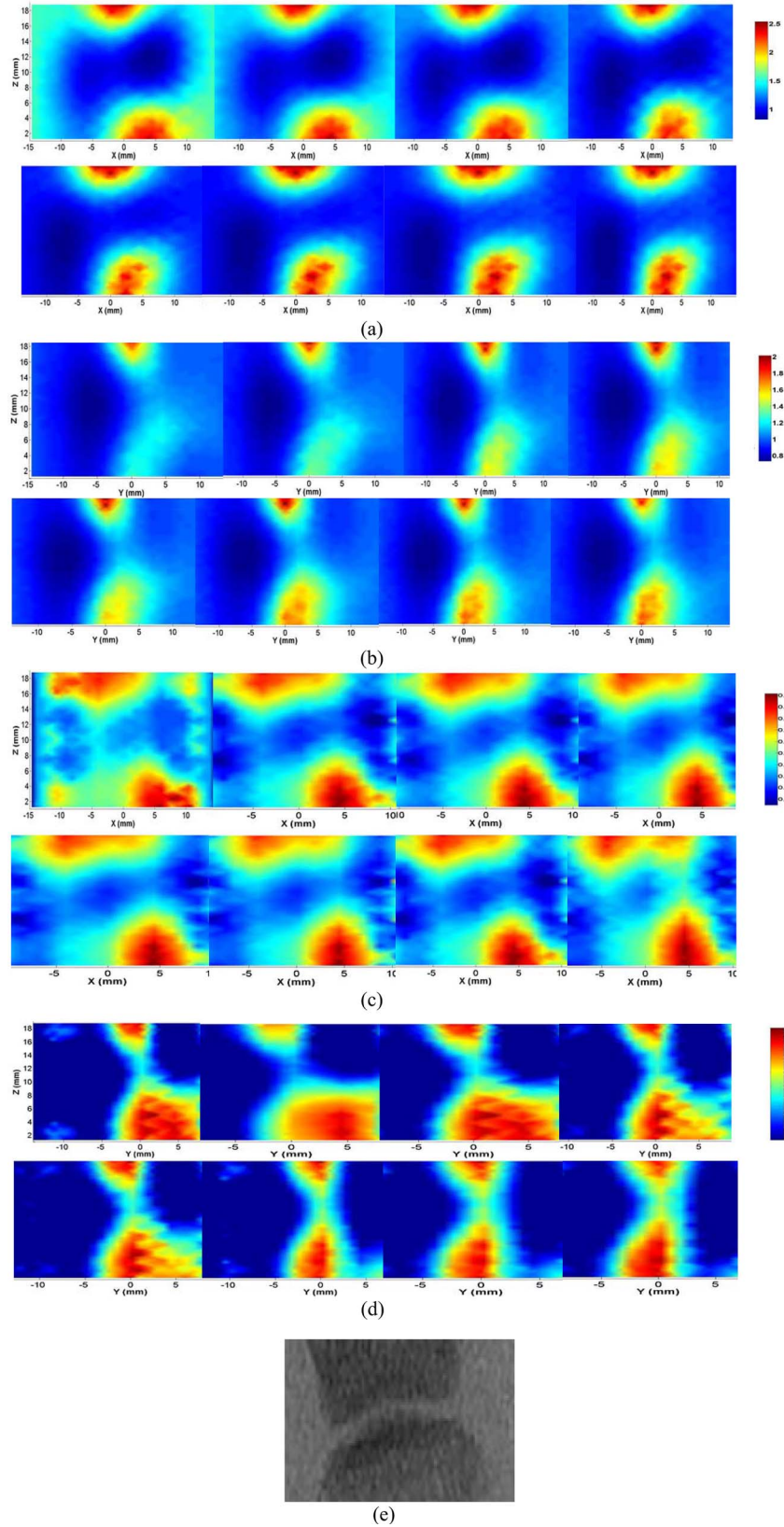


Fig. 5 Reconstructed images at selected dorsal/coronal planes from case 3: (a) scattering slices at $y = -3, -2, -1.5, -1, -0.5, 0, 1,$ and 1.5 mm (dorsal planes); (b) scattering slices at $x = -1, -0.5, 0, 0.5, 1.0, 1.5, 2,$ and 3 mm (coronal planes); (c) absorption slices at $y = -3, -2, -1.5, -1, -0.5, 0, 1,$ and 1.5 mm (dorsal planes); (d) absorption slices at $x = -1, -0.5, 0, 0.5, 1.0, 1.5, 2,$ and 3 mm (coronal planes); and (e) the x-ray image.

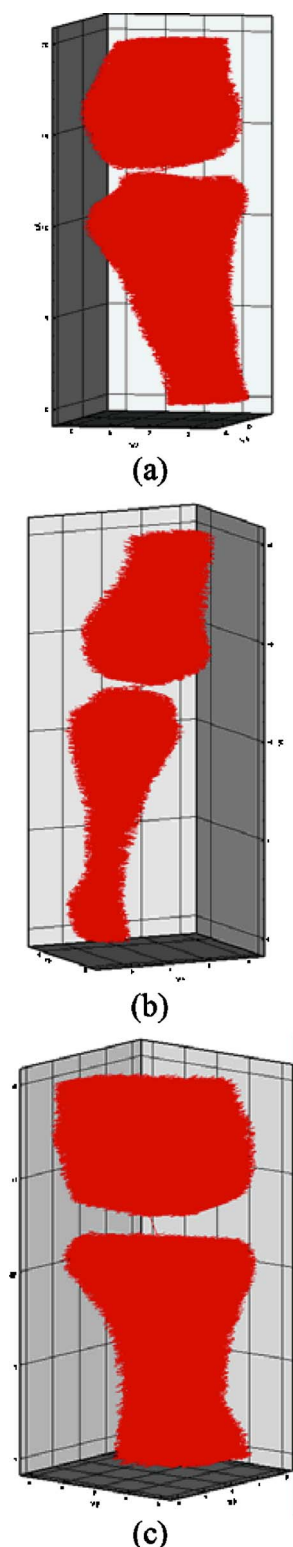


Fig. 6 Reconstructed 3-D tomosynthesis x-ray images: (a) case 1; (b) case 2; and (c) case 3.

diseased and healthy cartilages do not show clear differences. Again, we observe that the ratio of the absorption coefficient of the diseased cartilage and fluid to that of associated bone is also larger than this ratio for the normal controls. In addition,

as displayed in Table 2, the mean thickness of cartilage and fluid computed from the absorption property distributions are 1.0 and 0.3 mm, and 1.1 and 0.4 mm, respectively, for cases 1 and 2. However, the mean cartilage and fluid thickness for cases 3 to 5 are 1.8 and 0.5 mm, 1.3 and 0.4 mm, and 1.5 and 0.5 mm, respectively. Judging from the structural size parameters in Table 2, we find that the mean thickness of cartilage and fluid in the joints affected by OA seems to be thinner than healthy ones. We can also see from Tables 1 and 2 that the structural size computed from the absorption and scattering distributions are in general consistent with each other, except for case 4. The joint space narrowing observed from the optical images for the OA joints are also consistent with the x-ray findings [Figs. 3(e) and 4(e)]. It is noted from Tables 1 and 2 that the error of the recovered structural parameters is less than 30% compared to the x-ray findings. Although x-ray imaging is unable to show contrast for soft joint tissues, its high resolution ability for hardware tissue provides a standard for examining the structural information obtained from DOT. In this regard, we can conclude that the optical images presented in Figs. 3–5 are geometrically consistent with the x-ray images shown in Fig. 6.

It should be noted that although joint space narrowing is an important indicator for OA diagnosis, we cannot judge if this patient is really affected by this disease from only structural information, as natural variations exist between different individuals. Hence, we must employ both structural (space narrowing) and functional information (optical properties) to diagnose OA.

While we are confident about the accuracy of the recovered optical properties of the nonfluid regions, the accuracy of the properties for the fluid may be overestimated. This overestimation could be caused by the breakdown of the photon diffusion equation in the region of fluid, as it is well known that the scattering coefficient needs to be much larger than the absorption coefficient for the diffusion equation to be used accurately. We are currently implementing a 3-D reconstruction algorithm based on higher-order diffusion equations, which should eliminate such errors, as we have shown in 2-D reconstruction.³⁹

In summary, we report the first application of diffuse optical tomography to the assessment of OA in finger joints. OA-induced joint narrowing is fully and quantitatively revealed by the DOT imaging. It is noted from reconstructed results that the optical properties as well as the size between OA and healthy joints are quite different, and both could be used to monitor the progression of early OA.

Acknowledgment

This research was supported in part by the National Institutes of Health (R01 AR048122).

References

1. P. Sarzi-Puttini, M. A. Cimmino, R. Scarpa, R. Caporali, F. Parazzini, A. Zaninelli, F. Atzeni, and B. Canesi, "Osteoarthritis: an overview of the disease and its treatment strategies," *Semin Arthritis Rheum.* **35**, 1–10 (2005).
2. D. J. Hart and T. D. Spector, "Definition and epidemiology of osteoarthritis of the hand: a review," *Osteoarthritis Cartilage* **8**(A), S2–S7 (2000).
3. G. Karsenty, "An aggrecanase and osteoarthritis," *N. Engl. J. Med.* **353**, 522–523 (2005).

4. S. S. Glasson, R. Askew, B. Sheppard, B. Carito, T. Blanchet, H. L. Ma, C. R. Flannery, D. Peluso, K. Kanki, Z. Yang et al., "Deletion of active ADAMTS5 prevents cartilage degradation in a murine model of osteoarthritis," *Nature (London)* **434**, 644–648 (2005).
5. H. Stanton, F. M. Rogerson, C. J. East, S. B. Golub, K. E. Lawlor, C. T. Meeker, C. B. Little, K. Last, P. J. Farmer, I. K. Campbell et al., "ADAMTS5 is the major aggrecanase in mouse cartilage in vivo and in vitro," *Nature (London)* **434**, 648–652 (2005).
6. M. Sabatini, C. Lesur, M. Thomas, A. Chomel, P. Anract, G. de Nanteuil, and P. Pastoureau, "Effect of inhibition of matrix metalloproteinases on cartilage loss in vitro and in a guinea pig model of osteoarthritis," *Arthritis Rheum.* **52**, 171–180 (2005).
7. H. Nagase and M. Kashiwagi, "Aggrecanases and cartilage matrix degradation," *Arthritis Res. Ther.* **5**, 94–103 (2003).
8. M. A. D'Agostino, P. Conaghan, M. Le Bars, G. Baron, W. Grassi, E. Martin-Mola, R. Wakefield, J. L. Brasseur, A. So, M. Backhaus, M. Malaise, G. Burmester, N. Schmidely, P. Ravaud, M. Dougados, and P. Emery, "EULAR report on the use of ultrasonography in painful knee osteoarthritis. Part 1: Prevalence of inflammation in osteoarthritis," *Ann. Rheum. Dis.* **64**, 1703–1709 (2005).
9. W. P. Chan, P. Lang, M. P. Stevens, K. Sack, S. Majumdar, D. W. Stoller, C. Basch, and H. K. Genant, "Osteoarthritis of the knee: comparison of radiology, CT, and MR imaging to assess extent and severity," *AJR, Am. J. Roentgenol.* **157**, 799–806 (1991).
10. P. Conaghan, M. A. D'Agostino, P. Ravaud, G. Baron, M. Le Bars, W. Grassi, E. Martin-Mola, R. Wakefield, J. L. Brasseur, A. So, M. Backhaus, M. Malaise, G. Burmester, N. Schmidely, P. Emery, and M. Dougados, "EULAR report on the use of ultrasonography in painful knee osteoarthritis. Part 2: Exploring decision rules for clinical utility," *Ann. Rheum. Dis.* **64**, 1710–1714 (2005).
11. J. A. Tyler, P. J. Watson, H. L. Herrod, M. Robson, and L. D. Hall, "Detection and monitoring of progressive cartilage degeneration of osteoarthritic cartilage by MRI," *Acta Orthop. Scand. Suppl.* **266**, 130–138 (1995).
12. M. Forman, R. Malamet, and D. Kaplan, "A survey of osteoarthritis of the knee in the elderly," *J. Rheumatol.* **10**, 282–287 (1983).
13. C. G. Peterfy, "Scratching the surface. Articular cartilage disorders of the knee," *MRI Clin. N. Am.* **8**, 409–430 (2000).
14. J. T. Sharp, "Assessment of radiographic abnormalities in rheumatoid arthritis: what have we accomplished and where should we go from here," *J. Rheumatol.* **22**, 1787–1791 (1995).
15. M. Ostergaard, M. Stoltenberg, P. Lovgreen-Nielsen, B. Volck, C. H. Jensen, and I. B. Lorenzen, "Magnetic resonance imaging determined synovial membrane and joint effusion volumes in rheumatoid arthritis and osteoarthritis," *Arthritis Rheum.* **40**, 1856–1867 (1997).
16. E. Naredo, I. Moller, C. Moragues, J. J. de Agustin, A. K. Scheel, W. Grassi, E. de Miguel, M. Backhaus, P. Balint, G. A. W. Bruyn, M. A. D'Agostino, E. Filippucci, A. Iagnocco, D. Kane, J. M. Koski, L. Mayordomo, W. A. Schmidt, W. A. A. Swen, M. Szkudlarek, L. Terslev, S. Torp-Pedersen, J. Uson, R. J. Wakefield, and C. Werner, "Interobserver reliability in musculoskeletal ultrasonography: results from a "Teach the Teachers" rheumatologist," *Ann. Rheum. Dis.* **65**, 14–19 (2006).
17. R. J. Wakefield, P. V. Balint, M. Szkudlarek, E. Filippucci, M. Backhaus, M. A. D'Agostino, E. N. Sanchez, A. Iagnocco, W. A. Schmidt, G. Bruyn, D. Kane, P. J. O'Connor, B. Manger, F. Joshua, J. Koski, W. Grassi, M. N. D. Lassere, N. Swen, F. Kainberger, A. Klauser, M. Ostergaard, A. K. Brown, K. P. Machold, and P. G. Conaghan, "Musculoskeletal ultrasound including definitions for ultrasonographic pathology," *J. Rheumatol.* **32**, 2485–2487 (2005).
18. H. Jiang, N. Iftimia, Y. Xu, J. Eggert, L. Fajardo, and K. Klove, "Near-infrared optical imaging of the breast with model-based reconstruction," *Acad. Radiol.* **9**, 186–194 (2002).
19. A. P. Gibson, J. C. Hebden, and S. R. Arridge, "Recent advances in diffuse optical imaging," *Phys. Med. Biol.* **50**, R1–R43 (2005).
20. Y. Xu, N. Iftimia, H. B. Jiang, L. L. Key, and M. B. Bolster, "Three-dimensional diffuse optical tomography of bones and joints," *J. Biomed. Opt.* **7**(1), 88–92 (2002).
21. A. H. Hielscher, A. D. Klose, A. K. Scheel, B. Moa-Anderson, M. Backhaus, U. Netz, and J. Beuthan, "Sagittal laser optical tomography for imaging of rheumatoid finger joints," *Phys. Med. Biol.* **49**, 1147–1163 (2004).
22. A. Pifferi, A. Torricelli, P. Taroni, A. Bassi, E. Chikoidze, E. Giambattistelli, and R. Cubeddu, "Optical biopsy of bone tissue: a step toward the diagnosis of bone pathologies," *J. Biomed. Opt.* **9**(3), 474–480 (2004).
23. Y. Xu, N. Iftimia, and H. Jiang, "Imaging of in vitro and in vivo bones and joints with continuous-wave diffuse optical tomography," *Opt. Express* **8**, 447–451 (2001).
24. A. Schwaighofer, V. Tresp, P. Mayer, A. Krause, J. Beuthan, H. Rost, G. Metzger, G. A. Muller, and A. K. Scheel, "Classification of rheumatoid joint inflammation based on laser imaging," *IEEE Trans. Biomed. Eng.* **50**, 375–382 (2003).
25. A. K. Scheel, A. Krause, Rheinbaben I. Mesecke-von, G. Metzger, H. Rost, V. Tresp, P. Mayer, M. Reuss-Borst, and G. A. Müller, "Assessment of proximal finger joint inflammation in patients with rheumatoid arthritis using a novel laser-based imaging technique," *Arthritis Rheum.* **46**, 1177–1184 (2002).
26. V. Prapavat, W. Runge, J. Mans, A. Krause, J. Beuthan, and G. Muller, "Development of a finger joint phantom for the optical simulation of early stages of rheumatoid arthritis," *Biomed. Tech.* **42**, 319–326 (1997).
27. A. Klose, V. Prapavat, O. Minet, J. Beuthan, and G. Mueller, "Investigations of RA diagnostics applying optical tomography in frequency-domain," *Proc. SPIE* **3196**, 194–204 (1997).
28. Q. Zhang and H. Jiang, "Three-dimensional diffuse optical tomography of simulated hand joints with a 64×64-channel photodiodes-based optical system," *J. Opt. A, Pure Appl. Opt.* **7**, 224–231 (2005).
29. Z. Yuan, Q. Z. Zhang, and H. B. Jiang, "3D diffuse optical tomography of finger joints based on globally convergent methods and enhanced initial values optimization scheme," *2006 Tech. Digest OSA Biomed. Opt. Top. Mtg.*, Fort Lauderdale, FL (2006).
30. C. Li and H. Jiang, "A calibration method in diffuse optical tomography," *J. Opt. A, Pure Appl. Opt.* **6**, 844–852 (2004).
31. N. Iftimia and H. Jiang, "Quantitative optical image reconstruction of turbid media by use of direct-current measurements," *Appl. Opt.* **39**, 5256–5261 (2000).
32. H. Jiang, K. D. Paulsen, U. Osterberg, B. Pogue, and M. Patterson, "Optical image reconstruction using frequency-domain data: simulations and experiments," *J. Opt. Soc. Am. A* **13**, 253–266 (1996).
33. K. D. Paulsen and H. Jiang, "Spatially-varying optical property reconstruction using a finite element diffusion equation approximation," *Med. Phys.* **22**, 691–701 (1995).
34. M. Michael, H. P. William, A. T. Saul, T. V. William, and P. F. Brian, *Numerical Recipes in Fortran 77*, Cambridge Univ. Press, Boston, MA (1992).
35. S. Li and H. Jiang, "A practical method for three-dimensional reconstruction of joints using a C-arm system and shift-and-add algorithm," *Med. Phys.* **32**, 1491–1499 (2005).
36. "AMIRA—Advanced Visualization-Data Analysis-Geometry Reconstruction," User's Guide, TGS Company.
37. J. Rogowska, C. M. Bryant, and M. E. Brezinski, "Cartilage thickness measurement from optical coherence tomography," *J. Opt. Soc. Am. A* **20**, 357–363 (2003).
38. M. D. Robson, R. J. Hodgson, N. J. Herrod, J. A. Tyler, and L. D. Hall, "A combined analysis and magnetic resonance imaging technique for computerized automatic measurement of cartilage thickness in the interphalangeal joint," *Magn. Reson. Imaging* **13**, 709–718 (1995).
39. H. Jiang, "Optical image reconstruction based on the third-order diffuse equations," *Opt. Express* **4**, 241–246 (1999).